AIAA 96–2089

Numerical Solution of Incompressible Navier–Stokes Equations Using a Fractional–Step Approach

Cetin Kiris
MCAT Inc., Mountain View, CA

Dochan Kwak
NASA Ames Research Center,Moffett Field, CA

27th AIAA Fluid Dynamics Conference
June 17–20, 1996 / New Orleans, LA

NUMERICAL SOLUTION OF INCOMPRESSIBLE NAVIER-STOKES EQUATIONS USING A FRACTIONAL-STEP APPROACH

Cetin Kiris*
MCAT, Inc., Mountain View, CA

and

Dochan Kwak**
NASA-Ames Research Center, Moffett Field, CA

Abstract

A fractional step method for the solution of steady and unsteady incompressible Navier-Stokes equations is outlined. The method is based on a finite-volume formulation and uses the pressure in the cell center and the mass fluxes across the faces of each cell as dependent variables. Implicit treatment of convective and viscous terms in the momentum equations enables the numerical stability restrictions to be relaxed. The linearization error in the implicit solution of momentum equations is reduced by using three subiterations in order to achieve second order temporal accuracy for time-accurate calculations. In spatial discretizations of the momentum equations, a high-order (3^{rd} and 5^{th}) flux-difference splitting for the convective terms and a second-order central difference for the viscous terms are used. The resulting algebraic equations are solved with a line-relaxation scheme which allows the use of large time step. A four color ZEBRA scheme is employed after the line-relaxation procedure in the solution of the Poisson equation for pressure. This procedure is applied to a Couette flow problem using a distorted computational grid to show that the method minimizes grid effects. Additional benchmark cases include the unsteady laminar flow over a circular cylinder for Reynolds Numbers of 200, and a 3-D, steady, turbulent wingtip vortex wake propagation study. The solution algorithm does a very good job in resolving the vortex core when 5^{th}-order upwind differencing and a modified production term in the Baldwin-Barth one-equation turbulence model are used with adequate grid resolution.

* Research Scientist, Senior Member AIAA

** Branch Cheif, Associate Fellow AIAA

1. Introduction

Numerical solution of the Incompressible Navier-Stokes (INS) equations requires special attention in order to satisfy the divergence-free constraint on the velocity field. One way to avoid the numerical difficulty is to use an artificial compressibility method.[1-5] With the artificial compressibility method, the elliptic-parabolic type equations are transformed into hyperbolic-parabolic type equations. Well-established solution algorithms developed for compressible flows can be utilized to solve the resulting equations. In addition, an unstaggered grid orientation can easily be incorporated in the artificial compressibility approach making the method simple and robust. Time-accurate solution of INS equations with artificial compressibility method requires, in a sense, the solution of a steady-state problem in order to advance one physical time step. This is possible with subiterating the equations in pseudo-time until divergence-free constraint on the velocity field is satisfied at each physical time step. When one needs to use small physical time step in time-accurate calculations in order to capture the details of the flow physics, the artificial compressibility approach can be costlier. In order to reduce the number of subiterations, one needs to experiment for the optimum range of the artificial compressibility coefficient, β. In theory, the artificial compressibility approach should give the same solution at the steady-state no matter what value of β is used. However, the value of β affects the convergence rate of the algorithm. Use of implicit and Newton-like iteration schemes reduces this problem substantially.[5] Further improvement in the convergence rate of artificial compressibility method for unsteady flows is an ongoing research effort.

An alternative to the artificial compressibilty method is a fractional step method, which is especially suitable for time-accurate calculations. In the fractional step method, the auxiliary velocity field is obtained by solving the momentum equations. Then, a Poisson equation for pressure is formed by taking the divergence of the momentum equations and by using a divergence-free velocity field constraint. The numerical solution of the Poisson equation for pres-

sure with the Neumann-type boundary conditions exists only if the compatibility condition is satisfied. In three-dimensional curvilinear coordinates, solving the resulting algebraic equations from Poisson and momentum equations efficiently is one of the important features of the fractional step method. Using staggered grid orientation might also be neccessary to satisfy the continuity equation.[6-13]

The staggered formulation of the fractional-step method has been successully applied in Cartesian coordinates.[7], but in a body-fitted curvilinear coordinates, the formulation is not straight-forward. Shvy *et al.*[8] attempted to develop a method for general geometry using contravariant-type velocity components in the correction step. Rosenfeld *et al.*[9-10] successfully developed a fractional-step solution procedure in curvilinear coordinates using the pressure and the mass fluxes, divided by constant density, across the faces of each cell as dependent variables. The resulting solver was validated using smoothly varying and nearly orthogonal grids. This solver was intented to be used for time-dependent flows requiring small physical time steps. However, there are CFL number restrictions for a wide variety of applications, and the method requires carefully generated grids without metric discontinuities and with very small streching ratios. In the present paper, the idea of solving the mass fluxes as dependent variables in momentum equations is used and the stability of the numerical method is greatly improved by treating both convective and viscous fluxes implicitly. The factorization error is removed by using a relaxation scheme to solve the algebraic equations. The time integration scheme and operator splitting technique are formulated such that overall second order temporal accuracy is mantained by reducing linearization error in the implicit procedure. The validation cases are selected to demonstrate that the solution procedure is robust under severe grid conditions with metric discontinuity. It is shown that large CFL numbers can be used for steady-state as well as time-accurate solutions. To demonstrate this capability, computed results for a wingtip wake vortex flowfield is presented in detail.

In the following section, the governing equations and the present fractional step algorithm for the solution of the incompressible Navier-Stokes equations will be outlined. Next, validation cases in two- and three-dimensional space will be presented.

2. Method of Solution

For simplicity, fractional-step procedure in section 2.2 is described in Cartesian coordinates. The formation of conservation of mass and momentum equations and their spatial discretizations are outlined in section 2.3. Section 2.4 details the turbulence model used in tip vortex wake propagation study.

2.1. Governing Equations

The unsteady, incompressible Navier-Stokes equations are comprised of mass conservation,

$$\frac{\partial u_i}{\partial x_i} = 0 \tag{1}$$

and momentum conservation equations.

$$\frac{\partial u_i}{\partial t} = -\frac{\partial p}{\partial x_i} - \frac{\partial u_i u_j}{\partial x_j} + \frac{\partial \tau_{ij}}{\partial x_j} = -\frac{\partial p}{\partial x_i} + R_i \tag{2}$$

In this case, t is the time, x_i the Cartesian coordinates, u_i the corresponding velocity components, and p the pressure. For a Newtonian fluid, the viscous stress tensor τ_{ij} can be written as

$$\tau_{ij} = \nu(\frac{\partial u_i}{\partial x_j} + \frac{\partial u_j}{\partial x_i}) \tag{3}$$

where ν is the effective kinematic viscosity.

2.2. Fractional-Step Procedure

The time integration scheme is based on operator splitting, which can be accomplished in several ways by combining the pressure, convective, and viscous terms in the momentum equations. The fractional step method, a projection method developed by Chorin[11], is based on the decomposition of vector field into a divergence free component and gradient of a scalar field. The common application of this method is done in two steps. The first step is to solve for an auxiliary velocity field using the momentum equations. In the second step, the velocity field is corrected by using the pressure which can map the auxiliary velocity onto a divergence free velocity field. The momentum equations are discretized in time using a three-point-backward difference formula:

$$\frac{1}{2\Delta t}(3u_i^* - 4u_i^n + u_i^{n-1}) = -\frac{\partial p^n}{\partial x_i} + R(u_i^*) \tag{4}$$

where u_i^* denotes the auxiliary velocity field. The $R(u_i^*)$ term in the momentum equations includes the convective and viscous terms. It should be noted that the time derivatives can be differenced using the Euler backward formula for steady-state calculations. The velocity field which satisfies the incompressibility condition has been obtained by using the following correction step.

$$\frac{1}{\Delta t}(\mathbf{u}^{n+1} - \mathbf{u}^*) = -\nabla p' \tag{5}$$

where $p' = p^{n+1} - p^n$. At $n+1$ time level, the velocity field has to satisfy the incompressibility condition which is the continuity equation.

$$\nabla \cdot \mathbf{u}^{n+1} = 0 \tag{6}$$

This incompressiblity condition is enforced by using a Poisson equation for pressure.

$$\nabla^2 p' = \frac{1}{\Delta t} \nabla \cdot \mathbf{u}^* \tag{7}$$

The Poisson equation for pressure is obtained by taking the divergence of equation (5) and using equation (6).

In equation (4), both convective and viscous terms are treated implicitly. In order to maintain second order temporal accuracy, the linearization error in the implicit solution of equation (4) needs to be reduced. This is achieved by using subiterations. In most cases, three subiterations are sufficient to reduce the linearization error. It should be noted that the purpose of subiteration procedure here is quite different than in the artificial compressibility method. Artificial compressibility formulation requires the solution of a steady-state problem at each physical time step. Therefore, the number of subiterations in an artificial compressibility approach can be an order of magnitude higher than number of subiterations for the present formulation.

2.3. Discretization

Since the spatial discretization is based on the finite-volume formulation, the governing equations will be written in the integral form for the conservation of mass

$$\oint_S \mathbf{u} \cdot d\mathbf{S} = 0 \tag{8}$$

and momentum.

$$\frac{\partial}{\partial t} \int_V \mathbf{u} dV = \oint_S (-\mathbf{uu} - p\mathbf{I} + \nu(\nabla \mathbf{u} + (\nabla \mathbf{u})^T)) \cdot d\mathbf{S} = \oint_S \bar{T} \cdot d\mathbf{S} \tag{9}$$

where $\mathbf{S}$ is the surface area vector, V is the cell volume, and $(.)^T$ is the transpoze operator. The discretization of the mass conservation equation (8) in finite volume formulation gives

$$\begin{aligned} &(\mathbf{S}^\xi \cdot \mathbf{u})_{j+\frac{1}{2},k,l} - (\mathbf{S}^\xi \cdot \mathbf{u})_{j-\frac{1}{2},k,l} + \\ &(\mathbf{S}^\eta \cdot \mathbf{u})_{j,k+\frac{1}{2},l} - (\mathbf{S}^\eta \cdot \mathbf{u})_{j,k-\frac{1}{2},l} + \\ &(\mathbf{S}^\zeta \cdot \mathbf{u})_{j,k,l+\frac{1}{2}} - (\mathbf{S}^\zeta \cdot \mathbf{u})_{j,k,l-\frac{1}{2}} = 0 \end{aligned} \tag{10}$$

The mass conservation equation is evaluated over the faces of a computational primary cell with volume $V_{j,k,l}$ which is shown for P_{jkl} in Figure 1-a. Each term in equation (10) approximates the mass flux over the corresponding cell face. If the mass fluxes are chosen as unknowns, the continuity equation is satisfied automatically in generalized coordinate systems. The mass fluxes over the ξ, η , and ζ faces of the computational cell are

$$\begin{aligned} U^\xi &= \mathbf{S}^\xi \cdot \mathbf{u} \\ U^\eta &= \mathbf{S}^\eta \cdot \mathbf{u} \\ U^\zeta &= \mathbf{S}^\zeta \cdot \mathbf{u} \end{aligned} \tag{11}$$

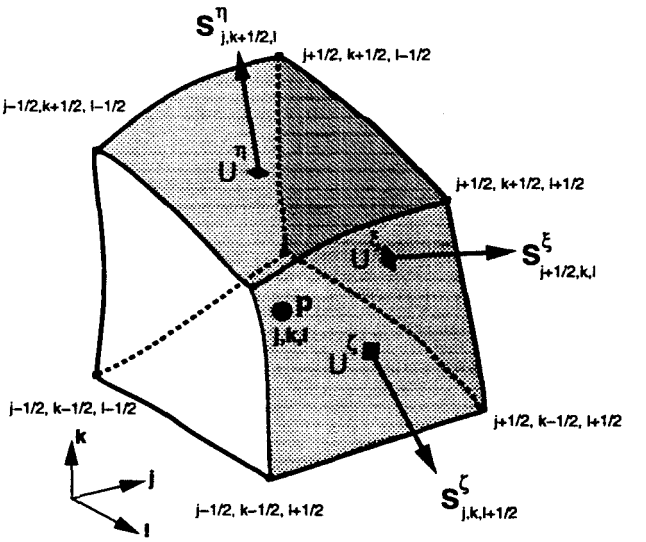

Figure 1-a. Schematic of a primary cell and staggered grid orientation.

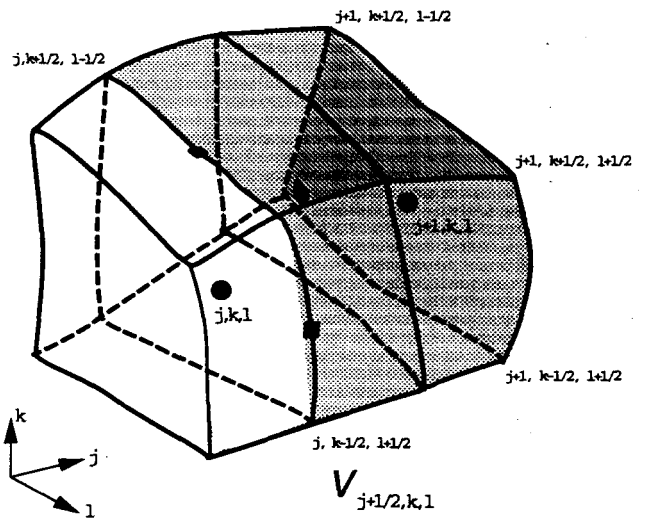

Figure 1-b. Computational cell for U^ξ momentum equation.

The continuity equation with this choice of the dependent variables takes a form identical to the Cartesian case. Therefore, the mass fluxes are considered as the 'natural' dependent variables for projection methods in curvilinear coordinates. The mass conservation equation with new dependent variables in a generalized coordinate system becomes

$$U^{\xi}_{j+\frac{1}{2},k,l} - U^{\xi}_{j-\frac{1}{2},k,l} + U^{\eta}_{j,k+\frac{1}{2},l} - U^{\eta}_{j,k-\frac{1}{2},l} + U^{\zeta}_{j,k,l+\frac{1}{2}} - U^{\zeta}_{j,k,l-\frac{1}{2}} = 0 \quad (12)$$

Treating the mass fluxes as dependent variables in finite volume formulation is equivalent to using contravariant velocity components, scaled by the inverse of the transformation Jacobian, in a finite-difference formulation. The mass fluxes in finite-volume discretization were used in references 9 – 10, and contravariant velocity components in finite-difference discretization were used in reference 12. The choice of mass fluxes as dependent variables complicates the discretization of the momentum equations. In order to replace $\mathbf{u}$ by the new dependent variables U^l, the corresponding area vectors are dotted with the momentum equations. Then the integral momentum equation is evaluated on different computational cells for each unknown U^l. Each cell has the dimensions of $\Delta\xi \times \Delta\eta \times \Delta\zeta$, but the centers are located at $(j+\frac{1}{2}, k, l)$, $(j, k+\frac{1}{2}, l)$, and $(j, k, l+\frac{1}{2})$ for U^{ξ}, U^{η}, and U^{ζ} momentum equations, respectively. The computational cell with volume $V_{j+1/2,k,l}$ for U^{ξ}-momentum equation is shown in Figure 1-b. The staggered grid orientation eliminates pressure checker-board-like oscillations in pressure and provides more compact stencils. The derivation of U^{ξ}-momentum equation will be outlined in this section. The U^{η}-, and U^{ζ}-momentum equations can be obtained by using cyclic permutation. Spatial discretization of the momentum conservation law equation (9) for a computational cell with volume V yields

$$\frac{\partial(Vu)}{\partial t} = \sum \mathbf{S}^l \cdot \bar{T} \quad (13)$$

The dot product of equation (13) and $\mathbf{S}_{\xi}$ results in

$$\frac{\partial(VU^{\xi})}{\partial t} = \mathbf{S}^{\xi}_{j+\frac{1}{2},k,l} \sum \mathbf{S}^l \cdot \bar{T} \quad (14)$$

where the summation is over all the faces of a computational cell. It is to be noted that

$$\mathbf{u} = \mathbf{S}_{\xi} U^{\xi} + \mathbf{S}_{\eta} U^{\eta} + \mathbf{S}_{\zeta} U^{\zeta} \quad (15)$$

and

$$U^l = \mathbf{S}^l \cdot u = \mathbf{S}^l \cdot \mathbf{S}_m U^m \quad (16)$$

The invariance of the velocity vector requires:

$$\mathbf{S}^l \cdot \mathbf{S}_m = \delta_{lm} \quad (17)$$

where δ_{lm} is the Kronecker delta, and $\mathbf{S}^l$ is the inverse base to $\mathbf{S}_m$. A uniform velocity field can be numerically preserved if the covariant base vector $\mathbf{S}_m$ is computed at each point from the relation

$$\mathbf{S}_m = (\mathbf{S}^{m+1} \times \mathbf{S}_{m+2}) / (\mathbf{S}^m \cdot (\mathbf{S}^{m+1} \times \mathbf{S}_{m+1})) \quad (18)$$

which satisfies (17) identically. The variable m is the cyclic permutation of (ξ, η, ζ).
In constructing momentum equations, the product $\mathbf{S}^l \cdot \bar{T}$ should be computed for each face of each momentum equation (see equation 14). For example, the ξ face-center for the U^{ξ} momentum cell is located at (j, k, l). The flux over this face is computed from

$$(\mathbf{S}^l \cdot \bar{T})_{j,k,l} = (-U^{\xi} U^l \mathbf{S}^l - \mathbf{S}^{\xi} P + \mathbf{S}^{\xi} \cdot \nu(\nabla\mathbf{u} + (\nabla\mathbf{u})^T))_{j,k,l} \quad (19)$$

The conservative form of the velocity vector gradient is

$$\nabla\mathbf{u} = \frac{\oint_S \mathbf{u} dS}{V} \quad (20)$$

Applying equation (20) for the computation of $\nabla\mathbf{u}_{j,k,l}$ yields

$$\begin{aligned} \nabla\mathbf{u} = \frac{1}{V} (& \mathbf{S}^{\xi}_{j+\frac{1}{2},k,l} \mathbf{u}_{j+\frac{1}{2},k,l} - \mathbf{S}^{\xi}_{j-\frac{1}{2},k,l} \mathbf{u}_{j-\frac{1}{2},k,l} \\ & + \mathbf{S}^{\eta}_{j,k+\frac{1}{2},l} \mathbf{u}_{j,k+\frac{1}{2},l} - \mathbf{S}^{\eta}_{j,k-\frac{1}{2},l} \mathbf{u}_{j,k-\frac{1}{2},l} \\ & + \mathbf{S}^{\zeta}_{j,k,l+\frac{1}{2}} \mathbf{u}_{j,k,l+\frac{1}{2}} - \mathbf{S}^{\zeta}_{j,k,l-\frac{1}{2}} \mathbf{u}_{j,k,l-\frac{1}{2}}) \end{aligned} \quad (21)$$

The η and ζ face centers are located at $(j+1/2, k-1/2, l)$ and $(j+1/2, k, l-1/2)$, respectively. The fluxes over these faces are computed in a similar way. The convective and viscous fluxes in equation (19) may be approximated in various ways. In the present work, the viscous fluxes are computed by simple averaging which results in second order central differencing. The convective flux terms, $U^{\xi} U^l \mathbf{S}^l$ in equation (19), are computed using higher-order upwind-biased stencil. Flux-difference splitting is used here to structure the differencing stencil based on the sign of the eigenvalues of the convective flux Jacobian. The numerical flux $\tilde{f}_{j+1/2}$ for the convective term in equation (19) is given by

$$\tilde{f}_{j+1/2} = \frac{1}{2} \left[f(\mathbf{u}_{j+1}) + f(\mathbf{u}_j) - \phi_{j+1/2} \right] \quad (22)$$

where the $\phi_{j+1/2}$ is a dissipation term. For $\phi_{j+1/2}$ = 0 this represents a second-order central difference scheme. A first-order upwind scheme is given by,

$$\phi_{j+1/2} = [\Delta f^{+}_{j+1/2} - \Delta f^{-}_{j+1/2}] \tag{23}$$

and a third-order upwind flux is defined by

$$\begin{aligned}\phi_{j+1/2} = -\frac{1}{3}[&\Delta f^{+}_{j-1/2} - \Delta f^{+}_{j+1/2} + \\ &\Delta f^{-}_{j+1/2} - \Delta f^{-}_{j+3/2}]\end{aligned} \tag{24}$$

A fifth-order-accurate, upwind-biased stencil which requires only seven points was derived by Rai[14] as follows

$$\begin{aligned}\phi_{j+1/2} = -\frac{1}{30}[&-2\Delta f^{+}_{j-3/2} + 11\Delta f^{+}_{j-1/2} \\ &-6\Delta f^{+}_{j+1/2} - 3\Delta f^{+}_{j+3/2} \\ &+2\Delta f^{-}_{j+5/2} - 11\Delta f^{-}_{j+3/2} \\ &+6\Delta f^{-}_{j+1/2} + 3\Delta f^{-}_{j-1/2}]\end{aligned} \tag{25}$$

where $\Delta f^{\pm}$ is the flux difference across positive or negative traveling waves. The flux difference is computed as

$$\Delta f^{\pm}_{j+1/2} = a^{\pm}(\bar{\mathbf{u}})\Delta \mathbf{u}_{j+1/2} \tag{26}$$

where the Δ operator is given by

$$\Delta \mathbf{u}_{j+1/2} = \mathbf{u}_{j+1} - \mathbf{u}_{j} \tag{27}$$

The plus (minus) Jacobian is computed from

$$a^{\pm} = \frac{1}{2}(a \pm |a|) \tag{28}$$

The Roe properties[15] which are necessary for a conservative scheme, are satisfied if the following averaging procedure is employed

$$\bar{\mathbf{u}} = \frac{1}{2}(\mathbf{u}_{j+1} + \mathbf{u}_{j}) \tag{29}$$

An implicit, delta-law form approximation to the momentum equations after linearization in time results in a hepta-diagonal scalar matrix equation written as

$$\begin{aligned}&\bar{b}\delta q_{j-1,k,l} + \bar{a}\delta q_{j,k,l} + \bar{c}\delta q_{j+1,k,l} + \bar{d}\delta q_{j,k-1,l} \\ &+\bar{e}\delta q_{j,k+1,l} + \bar{f}\delta q_{j,k,l-1} + \bar{g}\delta q_{j,k,l+1} = R.H.S.\end{aligned} \tag{30}$$

where $\delta q = U^{n+1} - U^{n}$ and $\bar{a}, \bar{b}, \bar{c}, \bar{d}, \bar{e}, \bar{f}$, and $\bar{g}$ are diagonals. The Gauss-Seidel line relaxation scheme, which was successfully employed by MacCormack[16], is used to solve the matrix equations. In Eq. (30), the right-hand-side term is computed and stored for the entire domain. The line relaxation procedure is composed of three stages, each stage involving a scalar tridiagonal inversion in one direction. In the first stage, δq is solved line-by-line in one direction. Before the tridiagonal equation is solved, off-tridiagonal terms are multiplied by the current value of δq and are shifted over to the right-hand-side of the equation. The same procedure is repeated in the second and third stage by inverting the tridiagonal matrix in one direction, and treating the off-diagonal terms for the other two directions in Gauss-Seidel fashion. One forward and one backward sweep in each computational direction is sufficient for most problems, but the number of sweeps can be increased.

A pressure Poisson equation for volume $V_{j,k,l}$ is formed by taking the divergence of the pressure gradient terms in momentum equations (see equation (19) and (5)). The resulting algebraic matrix equation in generalized curvilinear coordinates, contains nineteen diagonals. After two-sweeps of Gauss-Seidel line-relaxation procedure in each direction, a four color ZEBRA scheme, used in reference 9, is also utilized in the present work for the efficient solution of the Poisson equation.

2.4. Turbulence Model

The turbulent flow calculations use the one-equation turbulence model developed by Baldwin and Barth.[17] In this model, the transport equation for the turbulent Reynolds number is derived from a simplified form of the standard $k - \epsilon$ model equations. The model is relatively easy to implement because there is no need to define an algebraic length scale. The transport equation is solved by using the same Gauss-Seidel type line-relaxation scheme as the mean-flow equations. The details of this model can be found in reference 17. The wake-vortex calculations in section (3.3) use various approximations of the production term in the Baldwin-Barth one-equation model. The production term P for νR_T is given by

$$P \sim c\nu R_T X \tag{31}$$

where c is a constant, ν is the kinematic viscosity, R_T is the turbulent Reynolds number, and X is a scalar parameter which needs to be determined. Originally, the Baldwin-Barth one equation turbulence model was developed by using the magnitude of vorticity as X.

$$X = |\omega| \tag{32}$$

Spalart[18], and Dacles-Mariani[27] suggest to combine the magnitude of vorticity $|\omega|$ and the strain rate $|s| = (2S_{ij}S_{ij})^{1/2}$ as follows

$$X = |\omega| + xfactor(min(0, |s| - |\omega|)) \qquad (33)$$

In reference 27, $xfactor$ is set to 2.0 for tip vortex calcualtions. Another option for X is to use mimimum value of the magnitude of the vorticity and the norm of the strain rate tensor

$$X = min(|\omega|, ||\frac{1}{2}(\frac{\partial u_i}{\partial x_j} + \frac{\partial u_j}{\partial x_i})||) \qquad (34)$$

The computed results obtained using these production terms are compared in section 3.3.

3. Computed Results

Computed results for two laminar cases, and one turbulent case are presented in this section, Couette flow on a distorted grid, unsteady flow over a circular cyclinder, and a three-dimensional wingtip vortex wake flow are discussed. The wake-vortex calculations use the one-equation turbulence model developed by Baldwin and Barth.[17] The computer time requirement is 50.0×10^{-6} sec/grid point/iteration on Cray-C90 computer. Presently, the code has not been fully vectorized, so this figure will be reduced in the future.

3.1. Laminar Couette Flow

The first validation case is a grid quality study for laminar Couette flow, originally studied in reference 19. The computational grid with 63×63 mesh points is shown in Figure 2. The grid is intentionally generated in a saw-tooth shape to introduce metric discontinuity and non-orthogonality. Even with this "not-so-nice" mesh point distribution, the scheme should be able to resolve linear u- velocity profile which is the exact solution for the laminar Couette flow. The flow is started with freestream velocity everywhere except the stationary wall. The stationary wall has no-slip, and upper wall has a moving wall boundary condition. Inflow and outflow boundaries are periodic. CFL number of 100 is used for this computation, where the CFL number is defined as

$$CFL = max(|U^\xi| + |U^\eta| + |U^\zeta|) * dt/V \qquad (35)$$

Figure 3 shows axial (U) velocity contours at steady-state. The velocity contours show very small kinks where metric discontinuties are present in the mesh.

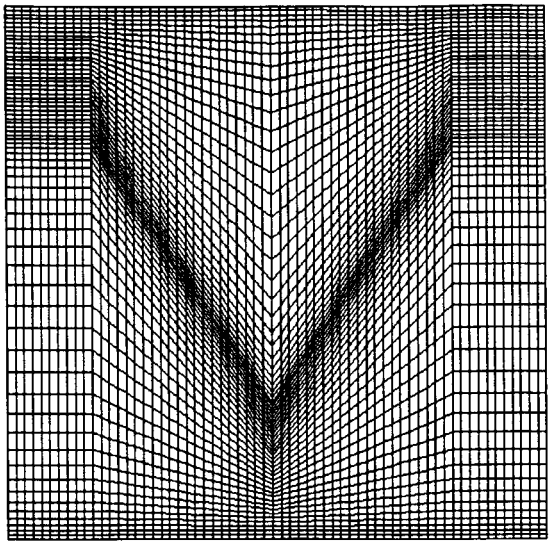

Figure 2 : Computational grid with 63x63 mesh points for Couette flow.

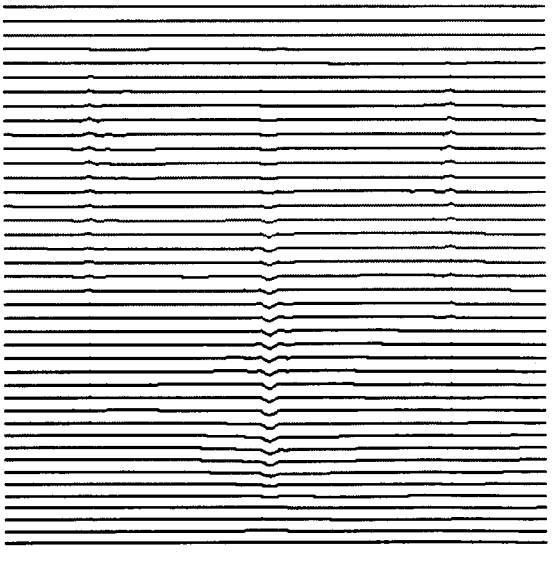

Figure 3 : U-velocity contours for Couette flow.

The $U-$ velocity profile at $x/L = 0.5$ station compares very well with the exact solution of the Couette flow, as shown in Figure 4. This case shows that the current approach introduces minimal grid effects where a sudden change in slope of grid lines occurs. The small grid quality errors that do arise have an insignificant effect on the solution shown in Figure 4.

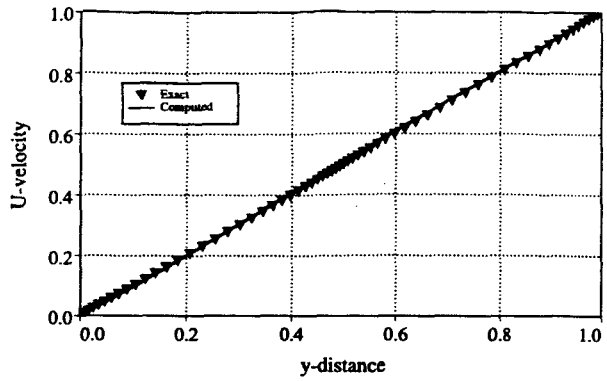

Figure 4 : U-velocity profile at for Couette flow.

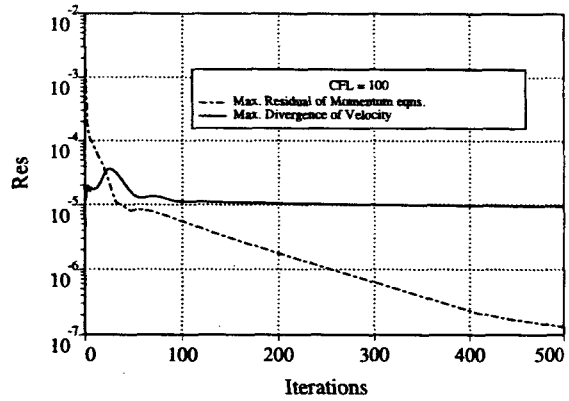

Figure 5 : Couette flow convergence history for present fractional-step formulation

The convergence history of the present method for this case is plotted in Figure 5. The solid line shows the maximum residual of the momentum equations, and the dashed line represents the maximum divergence of the velocity. The maximum divergence of velocity curve flattens about 10^{-5} value because the iteration procedure in the solution of the Poisson equation is terminated after achieving $\epsilon = 10^{-5}$ accuracy. With further iterations in the Poisson equation solution, the error in the divergence of velocity can be lowered to machine zero. Since this is a steady-state case, the Poisson equation has not been iterated beyond errors below 10^{-5}. It is observed that the convergence behavior of the existing method is good for this steady-state case with large CFL number. In addition, the divergence of velocity error is guaranteed below an ϵ value at each time step in fractional step method.

3.2. Vortex Shedding From a Circular Cylinder

The unsteady laminar vortex shedding from a circular cylinder at a Reynolds number of 200 was studied as a second test problem. The Reynolds number is based on the cylinder diameter and the free stream velocity. A 129x129 point O-type grid is used for this calculation, and the far field boundary is extended 15 diameters from the cylinder. The time step Δt of 0.025 was used and an ϵ value of 10^{-5} was set as a maximum error tolerance in the solution of Poisson equation. The flow was started impulsively from a free-stream condition and run until a periodic vortex shedding in the wake occured. The time evaluation of the lift and drag coefficients is plotted in Figure 6. The asymmetric wake started to develop within a nondimensional time of 40, and a nearly periodic solution is obtained by a nondimensional time of 100. The values of the aerodynamic coefficients for the periodic cycle are: $Cl = 0.0 \pm 0.67$ and $Cd = 1.26 \pm 0.04$. The Strouhal number can be calculated from the frequency of the oscillations for the lift coefficient and is found to be 0.184. Lift and drag coefficients and Strouhal number from the current computations are compared with numerical results by Rogers[4], Rosenfeld[9], Lecointe and Piquet[20], Martinez[21], Lin[22], Thoman and Szewczyk[23], and with experimental data by Experimental values by Wille[24], Kovasznay[25], and Roshko[26] in Table 1. The values of Strouhal number for computed results and experimental data are in the range of 0.160 and 0.227. Numerical results obtained from the current approach are closest to the artificial compressibilty results of Rogers[4] (5th order) even though the two methods are formulated quite differently. The present results also agree well with experimental data[24-26].

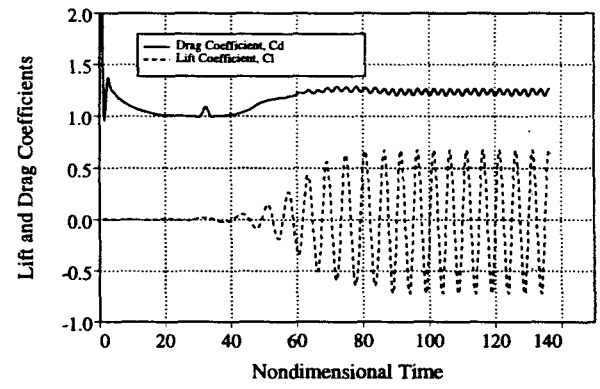

Figure 6 : Lift and drag coefficients versus time for flow over a circular cylinder at a Reynolds number of 200.

In Figure 7, particle traces and vorticity magnitude contours are plotted at various time during one period, which occurs over a nondimensional time of 5.43.

	Cl	Cd	St
Present	±0.67	1.26 ± 0.04	0.184
Rogers (num)			
3rd order	±0.75	1.29 ± 0.05	0.160
5th order	±0.65	1.23 ± 0.05	0.185
Rosenfeld (num)	±0.70	1.40 ± 0.04	0.201
Lecointe & Piquet (num)			
2nd order	±0.70	1.35 ± 0.04	0.227
4th order	±0.50	1.58 ± 0.0035	0.194
Martinez (num)		1.27 ± 0.0035	
Thoman & Szewczyk (num)		1.17 ± 0.005	
Wille (exp)		1.30	
Kovasznay (exp)			0.19
Roshko (exp)			0.19

Table 1 : Lift and drag coefficients for flow over a circular cylinder at a Reynolds number of 200.

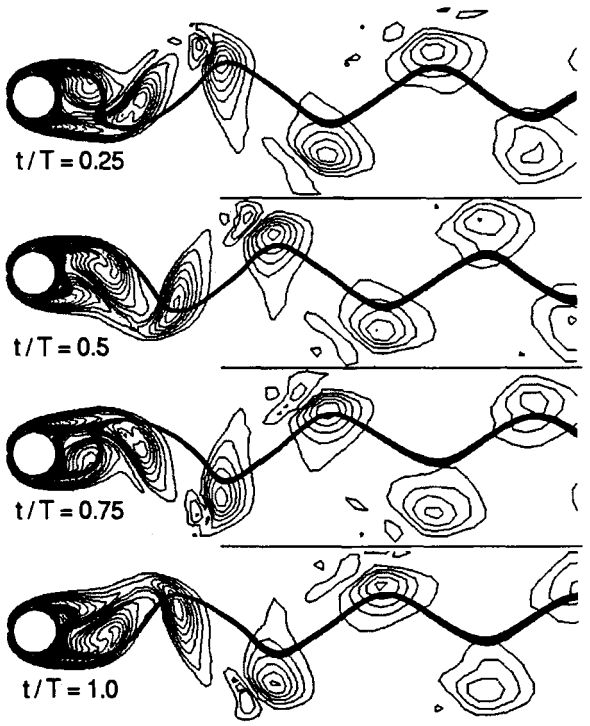

Figure 7 : Particle traces and vorticity magnitude contours for flow over circular cylinder at a Reynolds number of 200 at various nondimensional times.

The first plot shows the extension of the top vortex, resulting in maximum values of lift and drag. The next plot corresponds approximately to mimimum in drag with zero lift. The third and fourth plots are mirror images of the first two plots, corresponding approximately to maximum in drag with a minimum in lift and a minimum in drag with zero lift. Because of the contributions to the drag from both upper and lower vorticies forming behind the cylinder, the drag varies with double frequency compared to that of the lift.

3.3. Wake Vortex Propagation

The objective of this case is to investigate how a wingtip vortex is preserved in the present computational procedure. Since wingtip vorticies can exist for hundreds of chord-lengths behind the wing, a tip vortex generated by a large airplane can influence following aircraft. Blade/vortex interaction on rotorcraft and tip vortex cavitation on ship propeller blades are also areas where an accurate tip vortex simulation has a significant role. The computational study of the near-field behavior of a wingtip vortex using the artificial compressibility method,[27,28] done in conjuction with the experimental study,[29] indicated that it is possible to predict the mean flow with some degree of accuracy. It also has been shown that the success in capturing the flow features of the tip vortex depends on the grid resolution and the turbulence modeling. The static pressure coefficient in the vortex core was not predicted well, however, unless grid refinement in the core region was performed. One of the challenging problems in vortical flow simulation is to determine the source of numerical inaccuracy, whether it is from numerics, grid, or turbulence model. In order to isolate undesired grid effect from the turbulence modeling questions, Dacles-Mariani[27] studied wingtip vortex propagation using the artificial compressibility method. This wake vortex problem was selected as a validation case for the current fractional-step algorithm because of the challenging nature of the problem.

The schematic of the experimental test section and the computational domain with an H-H grid topology is shown in Figure 8. The wing has an aspect ratio of 0.75 and 10° angle of attack. The Reynolds number for this flow is 4.6 million based on the chord length. The computational domain includes the region from the trailing edge of the wing (x/c=1.0) to the 0.673 of the chordlength c, downstream of the wing. Extensive experimental data[29] is available at $x/c = 1.0$, $x/c = 1.12$, $x/c = 1.24$, $x/c = 1.447$, and $x/c = 1.673$. The experimental velocity profile at $x/c = 1.0$ station is used as inflow boundary conditions, and exit velocity components are extrapolated from the interior. Presure distributions at boundaries are calculated from the compatibility condition. The computations are carried out for two grid levels; a coarse grid which contains $36 \times 42 \times 42$ grid points, and a relatively fine grid with dimensions of $36 \times 82 \times 82$.

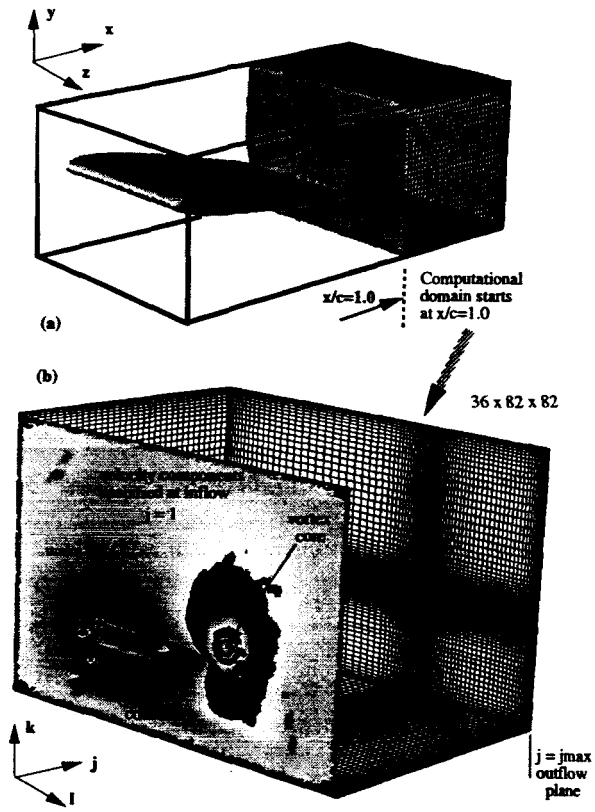

Figure 8 : Computational domain and grid for wake vortex flow calculations.

A typical convergence history for the coarse grid is plotted in Figure 9. The time step is set to 0.01 for this calculation. Dashed line shows the maximum changes in the dependent variables $\bar{U}^{\xi}$, $\bar{U}^{\eta}$, and $\bar{U}^{\zeta}$ momentum equations from time level n to $n+1$ (equations 4 and 5). The solid line represents the maximum value of divergence of the velocity error. The solution is considered converged in 1000 iterations. The CPU time required for this computation is less than one hour for coarse grid and about 3.5 CRAY-C90 hours for finer grid.

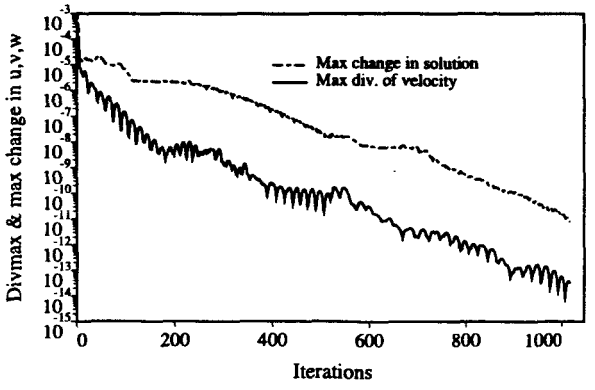

Figure 9: Convergence history for wake vortex calculation

Initially, the computations were carried out for the coarse grid. It was found that the vortex core velocity peak values were underpredicted. The grid resolution was inceased by doubling the number of grid points in k, and l direction, from grid dimension of $36 \times 42 \times 42$ to $36 \times 82 \times 82$. The prediction of the peak values at the vortex core was improved, but not substantially. The numerical results indicated that there is an excessive amount of numerical dissipation at the vortex core as it progresses downstream. This was consistent with the findings from the tip vortex study using artificial compressibility[27]. The excessive numerical diffusion at the vortex core was reduced when the production term in equation 32 is used instead of the magnitude of the vorticity (equation 31), as suggested by reference 27. It was observed that a numerical experimentation was necessary to find the right value of $xfactor$ in equation 32. In order to remove this dependency, the production term in equation 33, which is the minimum value of the magnitude of vorticity and the norm of the strain tensor, was used. A very good agreement obtained between the experimental data and computed results obtained by the last two approaches. Figures 10 through 14 compare computed results obtained from this procedure with the experimental data.

■	Experiment, Zilliac & Chow (1991)		
Computed results	**Convective terms diff..**	**Grid size j x k x l**	**Baldwin–Bart model production term**
———	3–rd upwind	36 x 82 x 82	min(|s| , |w|)
- - - -	5–th upwind	36 x 42 x 42	min(|s| , |w|)
.....	5–th upwind	36 x 82 x 82	|w|+2.0*min(0.0,|s|-|w|)
- • - •	5–th upwind	36 x 82 x 82	|w|
- - - •	5–th upwind	36 x 82 x 82	min(|s| , |w|)

Table 2 : Legend of the computed results presented in Figures 10 through 14

The legend for figures 10 through 14 is given in Table 2. Symbols represent the experimental data,[29] and lines represent the computed results. Chain-dotted lines show the results from 5^{th} order differencing from the coarse grid with dimensions of $36 \times 42 \times 42$. The production term in equation 33 was used for this case. Chain-dashed lines represent the results from the relatively fine grid with dimensions of $36 \times 82 \times 82$. The order of differencing and the production term are same as the previous case. Solid lines show the results from 3^{rd} order upwind differencing, keeping the grid size and the production term unchanged. Dotted lines show the results from the $36 \times 82 \times 82$ grid by using 5^{th} order differencing and using the production term in equation 32. The dashed lines represent the results by

using the production term in equation 31, which was originally used by Baldwin and Barth.

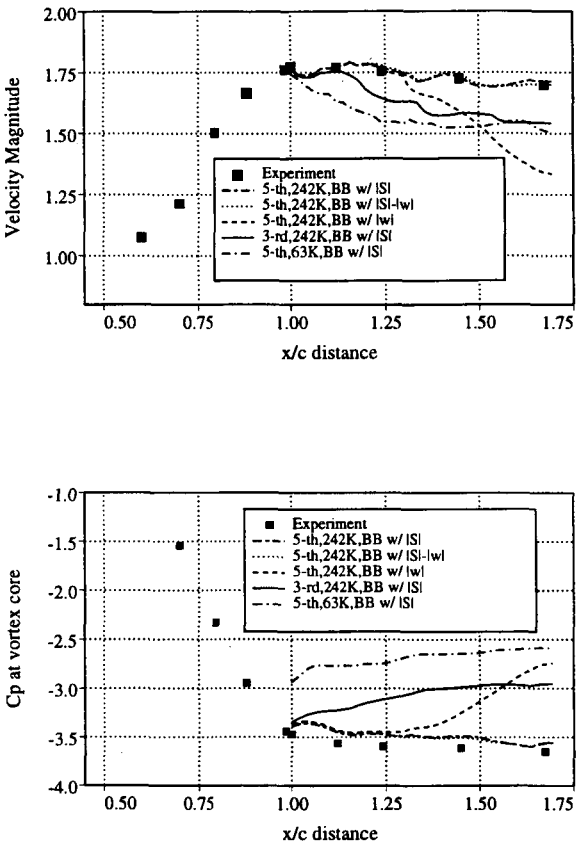

Figure 10 : Axial progression of flow quantites along vortex coreline.

Figure 10 shows the axial progression of flow quantities along vortex coreline. Velocity magnitude and static pressure coefficient Cp at the vortex core are plotted. The effect of the grid resolution (chain dotted lines) can be seen from these plots. Even though higher order of differencing and an improved production term in the turbulence model are used, the vortex core has not been resolved accurately with the coarse grid. When the grid resolution is increased the agreement between the numerical results and the experimental data is very good (chain-dashed lines), reducing the error in the viscous core region to less than 2%. The production terms in equation 32 and 33 give almost identical results (dotted and chain-dashed lines). However, the dashed lines clearly show the effects of the turbulence model. Using the magnitude of the vorticity in the production term gives excessive diffusion at the vortex core as it progresses downstream. The effect of order of differencing can be seen by comparing the solid lines with chain-dashed lines. The numerical dissipation is automatically computed in upwind differencing, and the amount of dissipation is large when third-order flux difference splitting is used at this grid level. In order to reduce this numerical dissipation, one can use finer grid or can increase the stencil in the upwind-biased differencing. Since the cost of increasing the accuracy of the differencing is much less than of increasing the grid size, the 5^{th} order upwind differencing is used for the rest of the cases. It should be pointed out that the overall spatial accuracy of the method is second-order even though 5^{th} order upwind differencing is used for convective terms. The reason for that is because the volume and surface area vector are evaluated as second-order, a simple averaging is used for the metric terms at half points location, and a second order central differencing is used for viscous terms. However, increasing the stencil in upwind differencing has a significant effect in reducng the amount of numerical dissipation, compared to lower-order differencing.

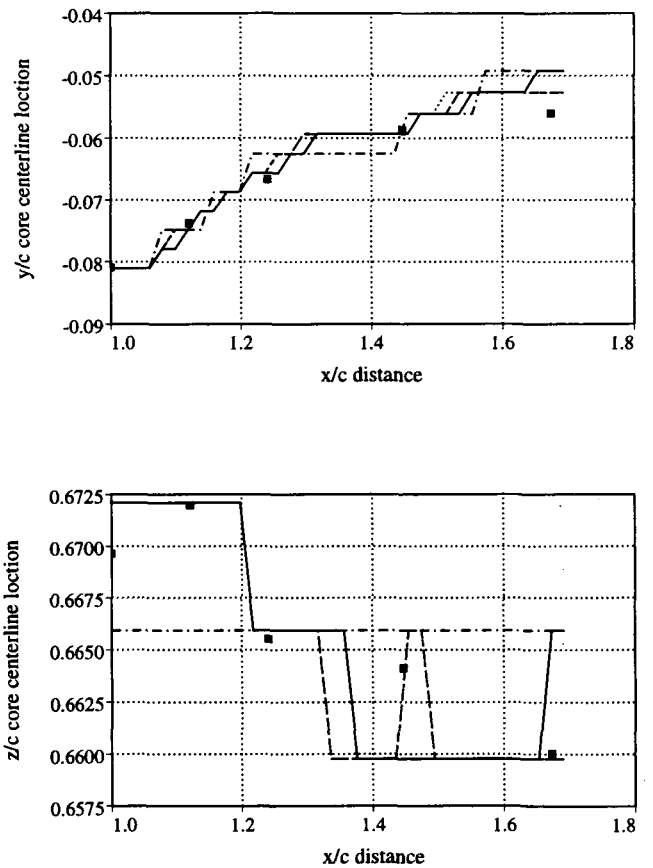

Figure 11: Axial progression of the vortex coreline

The vortex core location is plotted in Figure 11. In the coarse grid solution, the vortex core location

(z/c) remains unchanged because of the grid resolution. The use of various production terms in the turbulence model has a significant effect in the vortex core values (Figure 10). Figure 11 shows that vortex core location does not change with using different production terms. However, grid resolution and order of accuracy in the differencing have influence in location of the vortex coreline.

Figure 12 shows the comparison of velocity magnitude across the wake vortex at three interior stations ($x/c = 1.12$, $x/c = 1.24$, and $x/c = 1.447$) and at the exit boundary ($x/c = 1.673$). Since the experimental velocity profile is prescribed at the inflow boundary ($x/c = 1.0$), the results at $x/c = 1.0$ are not plotted. Resolving the vortex core peak values was the focus point for these calculations. As one can see from Figure 8, the grid resolution for the the wind tunnel wall boundary layer is not sufficient, especially for the Reynolds number of 4.6 Million. It should also be noted that the turbulence Reynolds number R_T in the Baldwin-Barth turbulence model is set to 1 at the inflow boundary. In actuality, the inflow boundary for the computational domain lies in the wake region for the experiment. Therefore, the boundary layer thickness on the wind tunnel wall is larger in the computed results than in the experimental measurments. This difference results in discrepancies between computed results and experimental data near the wind tunnel wall. The differences are the largest at the exit plane. Comparison of crossflow velocity across the wake vortex at four different stations is given in Figure 13. Using different production term in the turbulence model does not have a great influence in crossflow velocities as it has in the velocity magnitude (compare Figure 12 and 13). Since the crossflow velocity is zero at the vortex core, the dissipation introduced by the turbulence model, the grid spacing and the order of accuracy directly effects the axial velocity components. The comparison of Cp acros wake vortex at the inflow boundary, at one interior station ($x/c = 1.24$), and at the exit is plotted in Figure 14. Since the pressure has not been prescribed from experimental data, the computed Cp values are compared with the data at the inflow and the outflow boundaries. Obtaining a good comparison for the pressure at boundaries is especially encouraging for time-accurate comptations. The legend for computed results in these figures are given in Table 2. Dotted and chain-dashed lines show very good comparison with the experimental data. Findings from the previous figures about the effects of the grid resolution, order of accuraccy in differencing, and turbulence model are also valid for Cp plots.

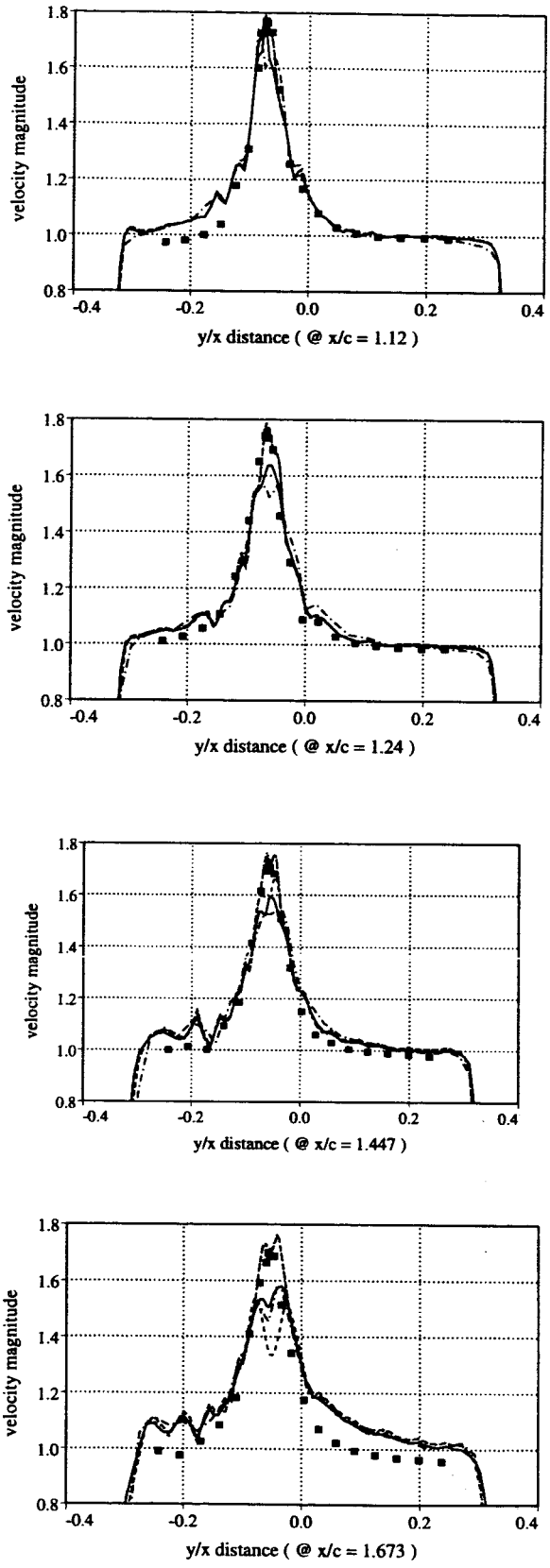

Figure 12: Comparison of velocity magnitude across wake vortex.

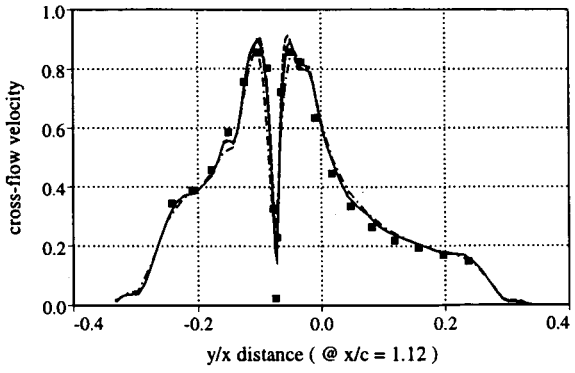

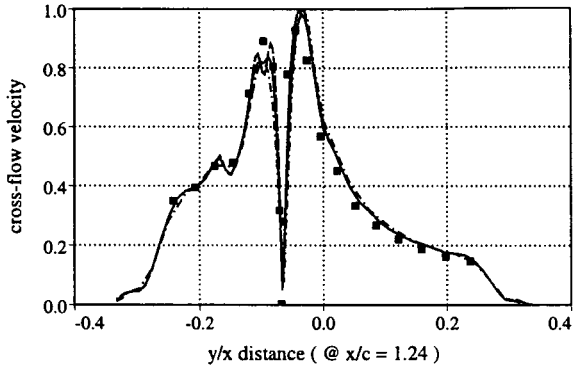

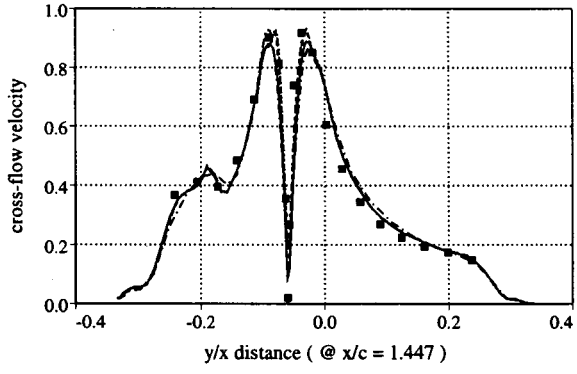

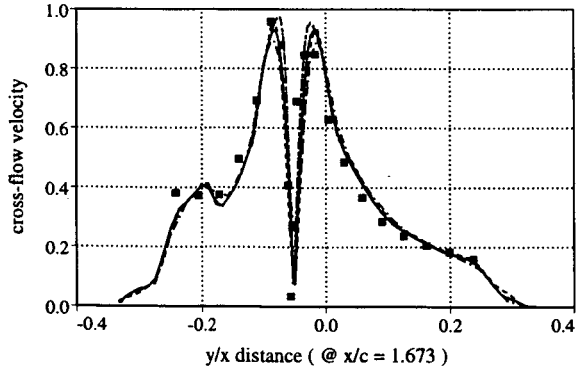

Figure 13: Comparison of crossflow velocity across wake vortex.

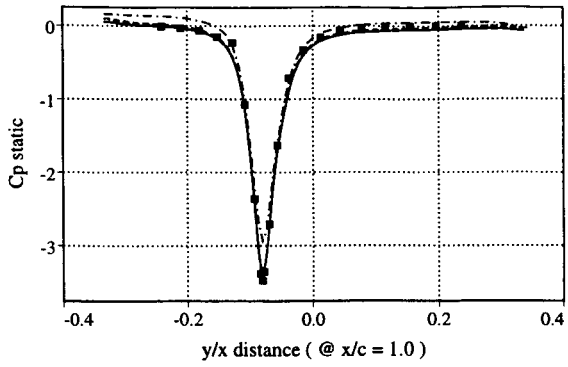

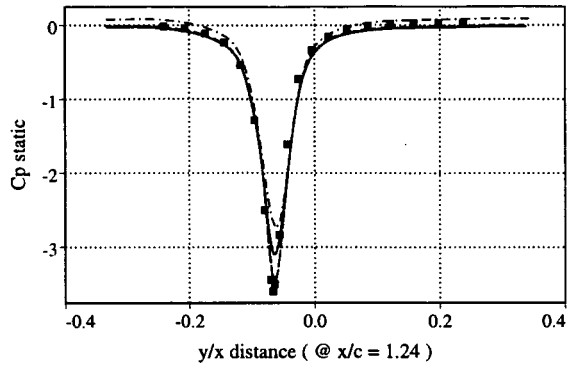

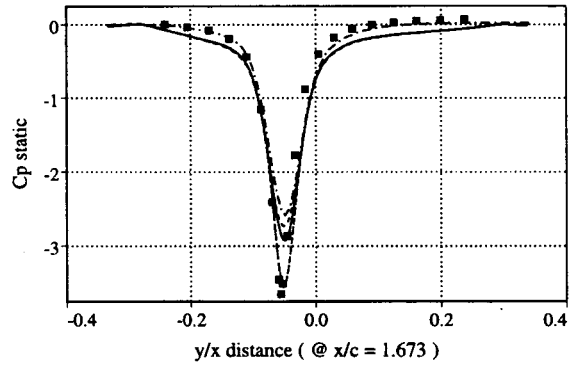

Figure 14: Comparison of Cp across wake vortex at inflow, exit and one interior station.

4.Conclusion

A fractional-step algorithm for computing both steady-state and time-accurate solutions to the incompressible Navier-Stokes equations has been presented. Using the mass fluxes as dependent variables in momentum equations automatically satisfies the incompressibility condition. The staggered grid orientation simplifies the pressure boundary condition in devising a Poisson solver and provides more compact stencils.

The use of upwind differencing with a non-factored implicit line-relaxation scheme in the solution of momentum equations provides fast convergence with relaxed stability restrictions.

The computed results showed good comparison with analytical solution of a laminar Couette flow and with experimental and other numerical results for an unsteady laminar flow over a circular cylinder. The validated solution procedure is applied to a three-dimensional, steady, turbulent wingtip vortex wake flow. The algorithm does a very good job in resolving the vortex core when 5^{th}-order upwind differencing and proper production term in the Baldwin-Barth one-equation turbulence model are used with adequate grid resolution.

Since the incompressibility condition is satisfied automatically at every physical time-step, the current fractional-step solver (INS3D-FS) will be applied to unsteady, three-dimensional flow problems.

Acknowledgments

The authors would like to thank G. Zilliac and J. Dacles-Mariani for providing the experimental data and the geometry for the wake-vortex problem. Computer time was provided by the Numerical Aerodynamic Simulation (NAS) Facility and the Central Computing Facility at NASA Ames Research Center.

References

1. Chorin, A., J., "A Numerical Method for Solving Incompressible Viscous Flow Problems," *Journal of Computational Physics,* Vol. 2, pp. 12-26, 1967.

2. Steger, J. L., Kutler, P., "Implicit Finite-Difference Procedures for the Computation of Vortex Wakes," *AIAA Journal* , Vol 15, no. 4, pp. 581-590, 1977.

3. Kwak, D., Chang, J. L C., Shanks, S. P., and Chakravarthy, S., "A Three-Dimensional Incompressible Navier-Stokes Flow Solver Using Primitive Variables," *AIAA Journal* , Vol. 24, No. 3, pp. 390-396, 1977.

4. Rogers, S. E., Kwak, D. "Upwind Differencing for the Time-Accurate Incompressible Navier-Stokes Equations," *AIAA Journal* , Vol. 28, No. 2, pp. 253-262, 1990.

5. Rogers, S. E., Kwak, D. and Kiris, C., "Numerical Solution of the Incompressible Navier-Stokes Equations for Steady and Time-Dependent Problems," *AIAA Journal* , Vol. 29, No. 4, pp. 603-610, 1991.

6. Harlow, F. H., and, Welch, J. E., "Numerical Calculation of Time-Dependent Viscous Incompressible Flow with Free Surface," *Phys. Fluids* , Vol. 8, No. 12, pp. 2182-2189, 1965.

7. Kim, J. and Moin, P., "Application of a Fractional-Step Method to Incompressible Navier-Stokes Equations," *J. Comp. Phys.* , Vol. 59, pp. 308-323, 1985.

8. Shvy, W., Tong, S. S., and Correa, S. M., "Numerical Recirculating Flow Calculation Using a Body-Fitted Coordinate System," *Num. Heat Transfer* , Vol. 8, pp. 99-113, 1985.

9. Rosenfeld, M., Kwak, D., and Vinokur, M., "A Fractional-Step Method for the Unsteady Incompressible Navier-Stokes Equations in Generalized Coordinate Systems," AIAA Paper No. 88-0718, 1988.

J. Comp. Physics , Vol. 94, No. 1, pp. 102-137, 1991.

10. Rosenfeld, M., and Kwak, D., "Numerical Solution of Unsteady Incompressible Viscous Flows In generalized Moving Coordinate Systems," AIAA Paper No. 89-0466, 1989.

11. Chorin, A. J., "On the Convergence of Discrete Approximations to the Navier-Stokes Equations," *Mathematics of Computation* , Vol. 23, pp. 341-353, 1969.

12. Choi, H., and Moin, P., "Effects of the Computational Time Step on Numerical Solutions of Turbulent Flow," *J. Comp. Phys.* , Vol. 113, pp. 1-4, 1994.

13. Gresho, P.M., and Chan, S.T., "An Update on Projection Methods for Transient Incompressible Viscous Flow," Sixth International Symposium on CFD, Lake Tahoe, Nevada, September 4-8, 1995

14 Rai, M. M. "Unsteady Three-Dimensional Navier-Stokes Simulations of Turbine Rotor-Stator Interaction," AIAA Paper No. 87-2058, 1987.

15 Roe, P.L., "Approximate Riemann Solvers, Parameter Vectors, and Difference Schemes," *Journal of Computational Physics,* Vol. 43, pp. 357-372 1981

16 MacCormack, R., W., "Current Status of Numerical Solutions of the Navier-Stokes Equations," AIAA Paper No. 85-0032, 1985.

17. Baldwin, B., S. and Barth, T., J., "A One-Equation Turbulence Transport Model for High Reynolds Number Wall-Bounded Flows," AIAA Paper No. 91-0610, 1991.

18. Spalart P., Allmaras, S., "A One-Equation Turbulence Transport Model for Aerodynamic Flows," AIAA Paper No. 92-0439, 1992.

19. Okamoto, K., K., "Assessing Grid Quality of Structured Meshes by Truncation Error Analysis," M.S. Thesis in ME, University of California, Davis, 1995.

20. Lecointe, Y., and Piquet, J., "On the Use of Several Compact Methods for the Study of Unsteady Incompressible Viscous Flow Around a Circular Cylinder," *Computers & Fluids* , Vol. 12, No. 4,pp. 255-280, 1984.

21. Martinez, G., *These D. I. I. N. P. Toulouse*, 1979.

22. Lin, C. L., Pepper, D. W., and Lee, S. C., "Numerical Methods for Separated Flow Sloutions

Around a Circular Cylinder," *AIAA j.* , Vol. 14, pp. 900-907, 1976.

23. Thoman, D., and Szewczyk, A., "Time Dependent Viscous Flow Over a Circular Cylinder," *Phys. Fluids, suppl. II* , pp. 79-86, 1969.

24. Wille, R., "Karman Vortex Streets," *Adv. Appl. Mech.*, , Vol. 6, pp. 273, 1960.

25. Kovasznay, L. S. G., "Hot-wire Investigation of the Wake Behind Cylinders at Low Reynolds Numbers," *Proc. Roy. Soc. A*, , Vol. 198, pp. 174-190, 1949.

26. Roshko, A., "On the Development of Turbulent Wakes From Vortex Streets," NACA Rep. 1191, 1954.

27. Dacles-Mariani, J., Rogers, S. E., Kwak, D., Zilliac, G., and Chow, J., "A Computational Study of Wingtip Vortex Flowfield," AIAA Paper No. 93-3010, 1993.

28. Dacles-Mariani, J., Zilliac, G., and Chow, J., Bradshaw, P., "Numerical/Experimental Study of Wingtip Vortex in the Near Field," *AIAA J.*, , Vol. 33, No. 9, pp. 1561-1568, 1995.

29. Chow, J., Zilliac, G., and Bradshaw, P., "Initial Roll-Up of a Wingtip Vortex," Proceedings of the Aircraft Wake Vortices Conference, Vol II, Washington, D.C., Oct. 29-31, 1991.